Correspondence and
requests for materials
should be addressed to
X.F. (feng@mpip-
mainz.mpg.de) or
K.M. (muellen@mpip-
mainz.mpg.de)

OPEN

Porous Iron Oxide Ribbons Grown on Graphene for High-Performance Lithium Storage

Shubin Yang, Yi Sun, Long Chen, Yenny Hernandez, Xinliang Feng & Klaus Müllen

Max Planck Institute for Polymer Research, Ackermannweg 10, D-55128 Mainz, Germany.

A well-designed nanostructure of transition metal oxides has been regarded as a key to solve their problems of large volume changes during lithium insertion-desertion processes which are associated with pulverization of the electrodes and rapid capacity decay. Here we report an effective approach for the fabrication of porous iron oxide ribbons by controlling the nucleation and growth of iron precursor onto the graphene surface and followed by an annealing treatment. The resultant iron oxide ribbons possess large aspect ratio, porous structure, thin feature and enhanced open-edges. These characteristics are favorable for the fast diffusion of lithium ions and electrons, and meanwhile can effectively accommodate the volume change of iron oxides during the cycling processes. As a consequence, the graphene-induced porous iron oxide ribbons exhibit a high reversible capacity and excellent cycle stability for lithium storage.

Transition metal oxides such as iron oxides[1], cobalt oxides[2] and molybdenum oxides[3] have attracted tremendous attention as anode materials for lithium ion batteries owing to their high theoretical capacities ($\sim$1000 mAh g^{-1}). In particular, iron oxides (Fe_2O_3 and Fe_3O_4) possess such abundant, inexpensive, and nontoxic properties so that they are regarded as the most promising candidates for lithium storage[4,5]. However, a large specific volume change commonly occurs in the host matrix of iron oxides during the cycling processes, resulting in pulverization of the electrodes and rapid capacity decay[4–6]. To circumvent these obstacles, one effective approach is to fabricate nanostructured iron oxides[7,8]. In well-designed nanostructures, not only the strain associated with volume change during lithium insertion and extraction processes can be accommodated, but also the lithium diffusion in electrodes becomes easy, leading to significantly improved electrochemical performance[7,9].

Two-dimensional nanosheets, such as graphene, metal chalcogenides, titania and manganese oxide[10–13] have been recently explored and shown improved host capabilities and cyclabilities for lithium storage owing to their limited volume change and short lithium diffusion pathway in matrix. In comparison, nanoribbons, stripes of nanosheets, can provide more open edges and active sites[14], which would enhance their reactivity toward Li adsorption as predicted by the recent computational studies[15]. However, the synthesis of nanoribbon materials, especially of electrochemically active metal oxide ribbons remains challenging.

In this article, we will demonstrate an efficient synthesis of porous iron oxide ribbons by controlling the nucleation and growth of iron glycolate onto the surface of graphene and followed by an annealing treatment in air. Reduced graphene oxide (RGO) is employed as a substrate[16–19], and iron acetylacetonate (FeAa)/ethylene glycol as the iron oxide precursor. The resulting iron oxide ribbons possess large aspect ratio, porous structure and thin feature. Such unique characteristics can not only provide numerous open channels for the access of electrolyte and thus facilitate the rapid diffusion of lithium ions from electrolyte to electrode, but can also effectively accommodate the volume change of iron oxides during the cycling processes. As a consequence, the porous iron oxide ribbons exhibit a high reversible capacity of 1050 mAh g^{-1} in the first 10 cycles, and over 1000 mAh g^{-1} after 130 cycles, holding great potential as an anode material for lithium storage.

Results
The overall synthetic procedure of porous iron oxide ribbons is schematically illustrated in Figure 1. Chemically reduced graphene oxide was first dispersed in a solution of ethylene glycol to create a dark suspension with the aid of a dispersant, polyvinylpyrrolidone (PVP). The suspension was then mixed with iron (II) acetylacetonate via ultrasonication, and then was heated to 170°C for the heterogeneous nucleation of the iron glycolate (FeG) (demonstrated in Figure S1a and S2) onto the surface of RGO. As presented in Figure S1, once the nucleation
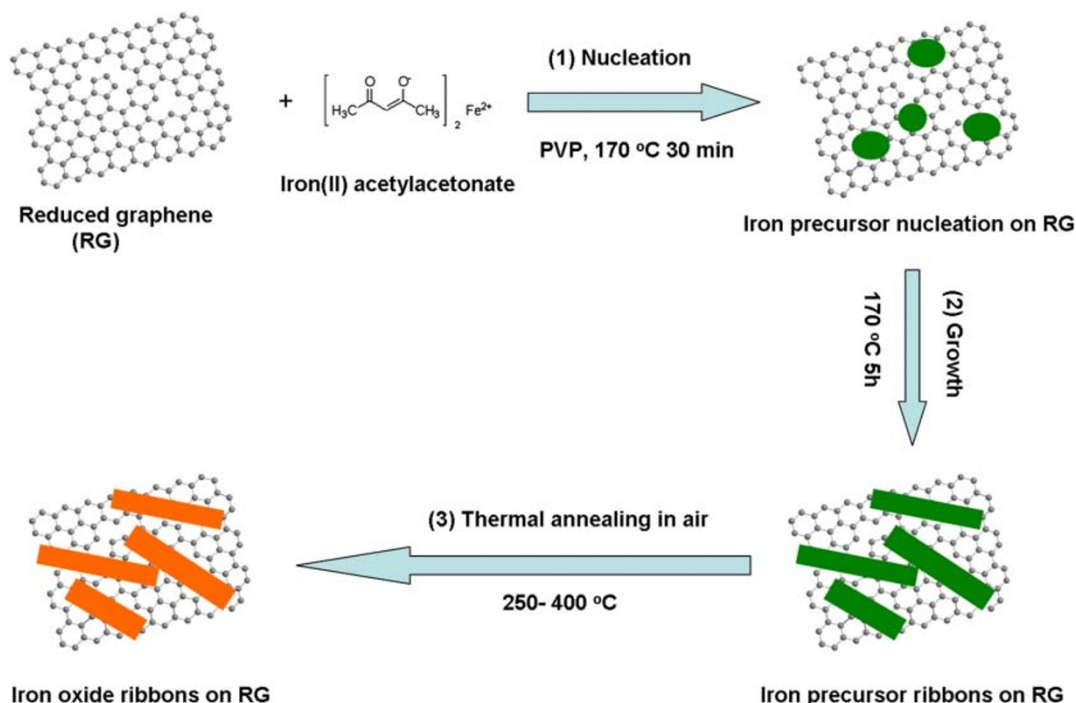
Figure 1 | Fabrication of iron oxide ribbons. It includes (1) and (2) controllable nucleation and growth of the iron glycolate onto the surface of the reduced graphene oxide at 170°C, and (3) thermal annealing at different temperatures (250–400°C) in air.

occurs, the residual iron precursor would further grow around the nucleus to form iron glycolate ribbons with various lengths when increasing the reaction time from 30 min to 5 h. Subsequent thermal annealing of the resulting ribbons at different temperatures (250–400°C) in air afforded the iron oxide ribbons, which are denoted as FeO-X; X represents the annealing temperature.

Characterization of iron glycolate ribbons. The morphology of the as-prepared iron glycolate ribbons was elucidated via transmission electron microscopy (TEM), scanning electron microscopy (SEM) and high-resolution TEM (HRTEM) measurements. As shown in Figure 2 and S3, a large number of ribbons with a width from 50 to 500 nm and a length from 600 nm to several micrometers on the surface of RGO can be observed. No other free ribbons or nanoparticles appear in the TEM and SEM visualizations. This result suggests that the complementary interaction between positively charged iron ions and negatively charged RGO can direct the growth of iron precursor ribbons on the surface of RGO during fabrication process. Such a proposed procedure can be further confirmed by our control experiments (see Supplementary Information, Figure S4), in which only iron precursor particles with irregular morphology are produced under the same synthesis conditions without adding reduced graphene oxide. Interestingly, the resulting ribbons possess numerous pores as displayed in the HRTEM images (Figure 2b and 2c). Closer inspection (Figure 2d) reveals that the porous architecture is built of fine particles with crystallite sizes of about 5 nm. Cross-sectional atomic force microscopy (AFM, Figure 2e and 2f) measurements were further conducted to reveal the structural features of the ribbons. Typical AFM analyses disclose the same morphology of ribbons as the observations from SEM and TEM, with a uniform thickness of about 50 nm.

Characterization of iron oxide ribbons. The as-prepared iron glycolate ribbons were then annealed at relatively low temperatures in air to generate iron oxide ribbons. Based on the element mapping analysis (Figure 3), we can recognize the uniform distribution of Fe and O elements in the iron oxide ribbons. Remarkably enough, when increasing the annealing temperature from 250 to 350°C, the porous

architecture of the iron oxide ribbons including crystalline size and porosity significantly changes (Figure 4), although their ribbon-like shape is almost the same as that of the sample before oxidation. In the case of FeO-250 ribbons, the obvious lattice fringes show the uniform interlayer distance of 0.25 nm as depicted in the HRTEM image (Figure 4c), in good agreement with the spacing between (311) planes of Fe_3O_4 crystals[9]. Such an assignment is further supported by its X-ray diffraction (XRD) patterns (Figure S5), in which the prominent diffraction peaks are perfectly indexed to Fe_3O_4 according to the standard card of Fe_3O_4 (JCPDS 88–0315)[4]. Notably, two weak peaks at 35.6 and 49.6° in the XRD patterns of FeO-250 ribbons are visible, which can be attributed to the (012) and (024) planes of Fe_2O_3, respectively (JCPDS 33–0664)[4]. The presence of Fe_2O_3 in FeO-250 ribbons should originate from the partial conversion of Fe_3O_4 during the annealing process since the diffraction peaks of Fe_2O_3 become more dominant when the annealing temperature is increased to 350°C (Figure S5). Such conversion phenomena are well consistent with the literatures[8,20]. In addition, we noted that thermal treatment of iron precursor ribbons at 400°C led to the complete transformation of Fe_3O_4 to pure α-Fe_2O_3 (see Supplementary Information, Figure S6).

The porous nature of iron oxide ribbons is further validated by nitrogen physisorption measurements. Their adsorption-desorption isotherm exhibits a type IV hysteresis loop at a relative pressure between 0.2 and 0.9 (Figure 5), characteristic for mesopores with different pore sizes. A Barrett-Joyner-Halenda (BJH) calculation discloses that the pore size distribution is in the range of 2–20 nm, in good agreement with that estimated from the TEM images. A specific surface area of 115 $m^2 g^{-1}$ can be derived, which is much higher than those reported for iron oxide/carbon composites (35–58 $m^2 g^{-1}$)[9,20] or iron oxide nanodiscs (52 $m^2 g^{-1}$)[7], and is even comparable to that reported for mesoporous iron oxides (116–128 $m^2 g^{-1}$)[21,22]. In combination with the analysis based on TEM and HRTEM images, it is reasonable to believe that the high surface area of iron oxide ribbons is due to its small crystal grains, which give rise to a porous architecture. Thermogravimetric analysis (TGA) (see Supplementary Information, Figure S7) reveals that the weight content of iron oxide in the composite is about 86 wt%. Such a high content of electrochemically
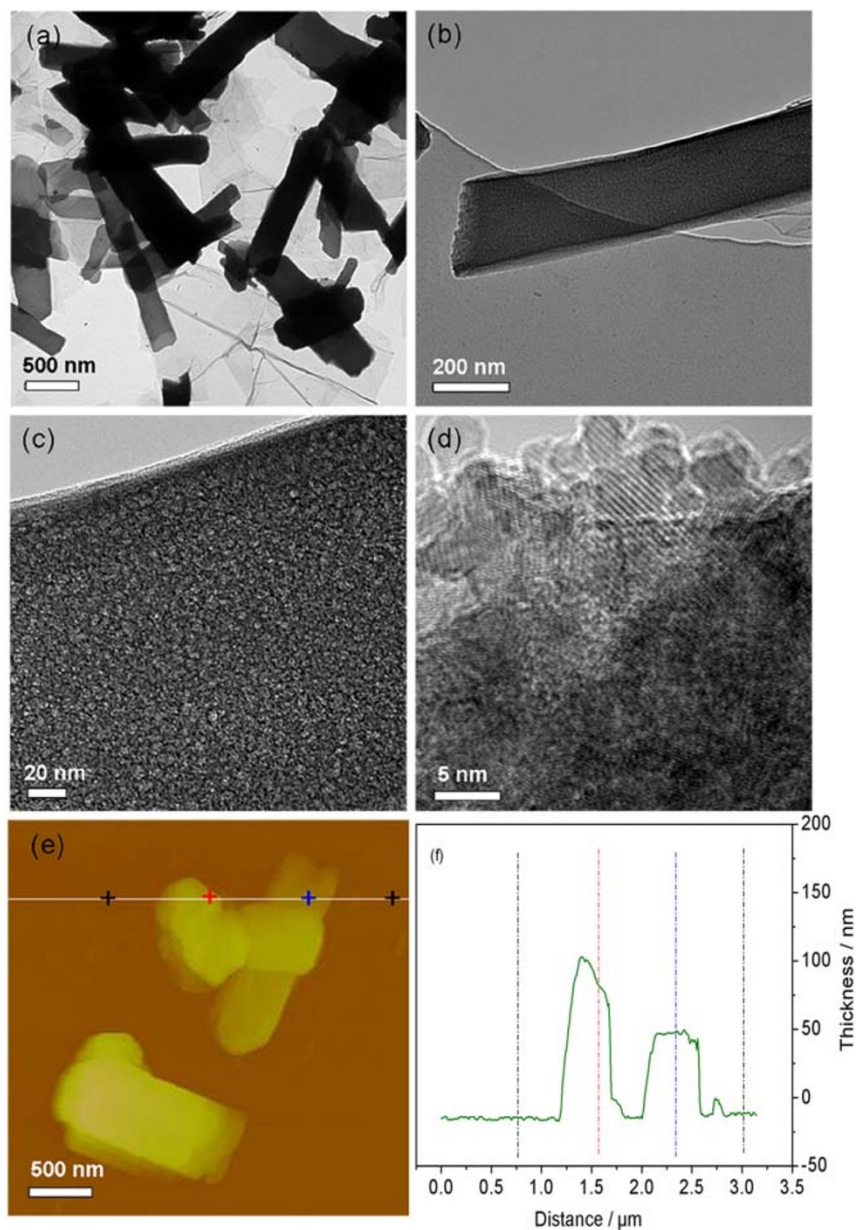
Figure 2 | Morphological and structural analysis of iron glycolate ribbons after growth for 5 h. (a–c) Typical TEM images with different magnifications. (d) HRTEM image reveal the monodispersed ribbons with porous architectures. (f) AFM image and the corresponding thickness analysis taken around the white line in (f) reveals a uniform thickness of about 50 nm.
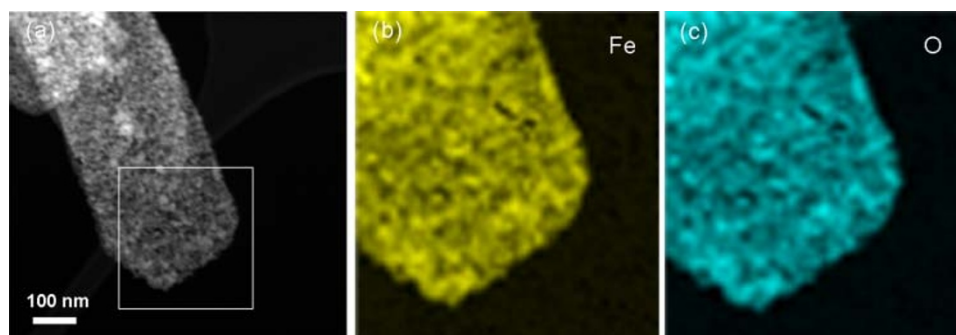
Figure 3 | Elemental mapping images of iron oxide ribbons. (a) Typical scanning transmission electron microscopy (STEM) image and corresponding elemental mapping images of (b) iron and (c) oxygen in the selected area (white rectangle in (a)), indicating the homogeneous dispersion of iron and oxygen in the FeO ribbons.
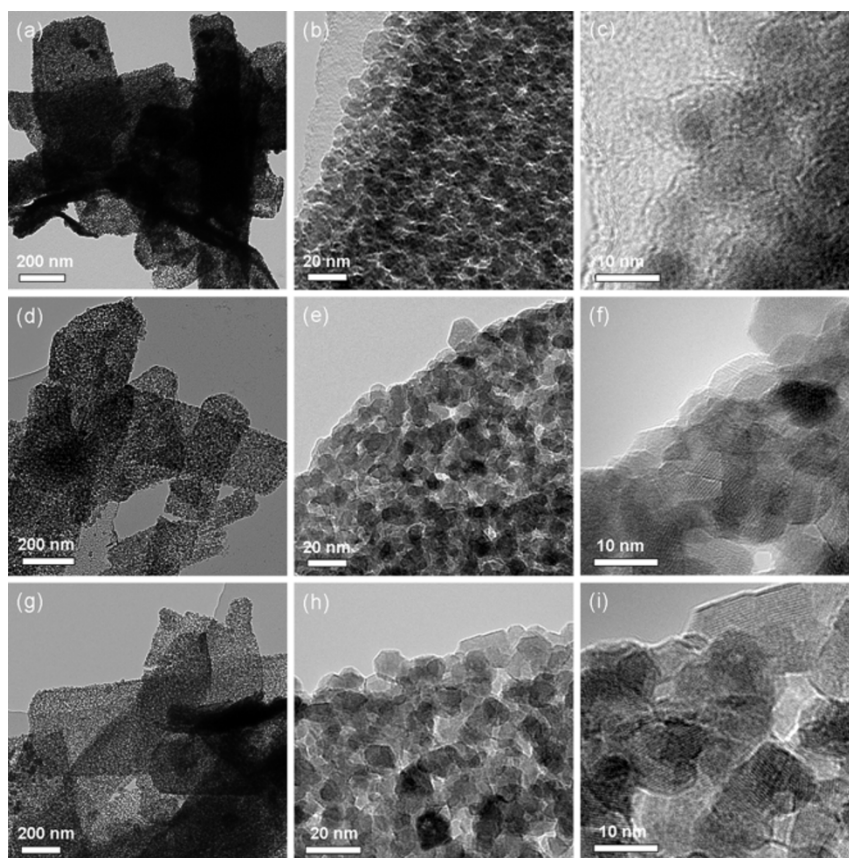
Figure 4 | Morphological and structural analysis of iron oxide ribbons annealed at various temperatures. (a,b) TEM images with different magnifications and (c) HRTEM image of FeO-250, (d,e) TEM images with different magnifications and (f) HRTEM image of FeO-300, (g,h) TEM images with different magnifications and (i) HRTEM image of FeO-350. It discloses that the annealing tempature can effectively tailor the nanostructure of iron oxide ribbons.

active iron oxide ribbons with a unique nanostructure should result in excellent electrochemical performance when they are applied as an anode material for lithium storage.

Electrochemical properties of iron oxide ribbons. The electrochemical performance of the iron oxide ribbons was evaluated by galvanostatic discharge (Li insertion)-charge (Li extraction) measurements at a current density of 74 mA g^{-1}. It is striking to note that a high first discharge capacity of 1426 mAh g^{-1} can be achieved (Figure 6a and 6b),

which largely exceeds the theoretical capacity of iron oxides ($\sim$1000 mAh g^{-1})[4,23]. This suggests the existence of additional lithium storagesites in the iron oxide ribbons. The detailed voltage profile analysis of the iron oxide ribbons demonstrates that three domains including an extended plateau and two slopes mainly contribute to the overall discharge capacity of FeO-250 ribbons during the discharge process. The first slope between 2.0 and 0.8 V corresponds to the lithium insertion into the nanocrystals of iron oxide and the conversion from Fe (III) to Fe (II)[21]. The long
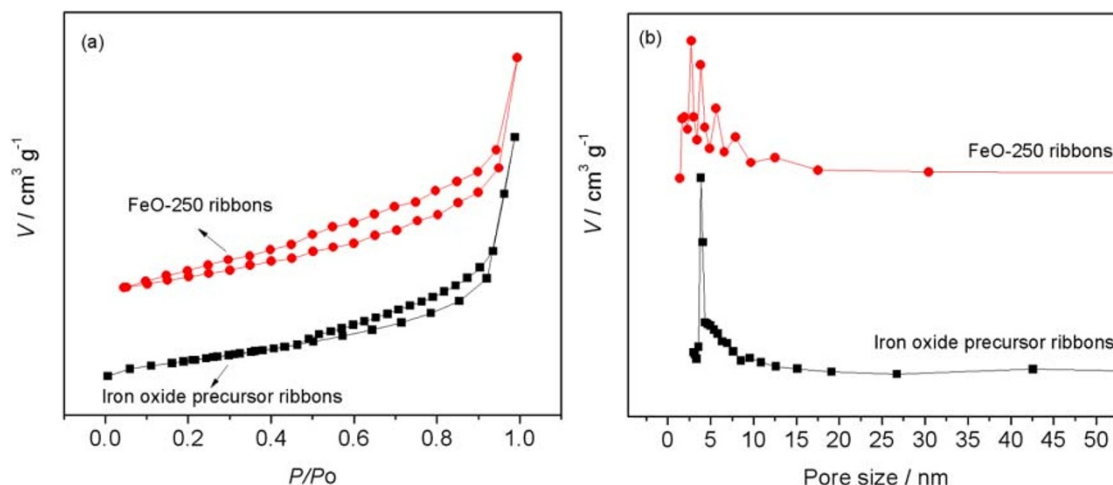

Figure 5 | Porous structure analysis of iron glycolate and iron oxide ribbons. (a) Nitrogen adsorption/desorption isotherm and (b) pore size distribution of iron glycolate and iron oxide ribbons, respectively, further demonstrate the porous structure with high surface area.
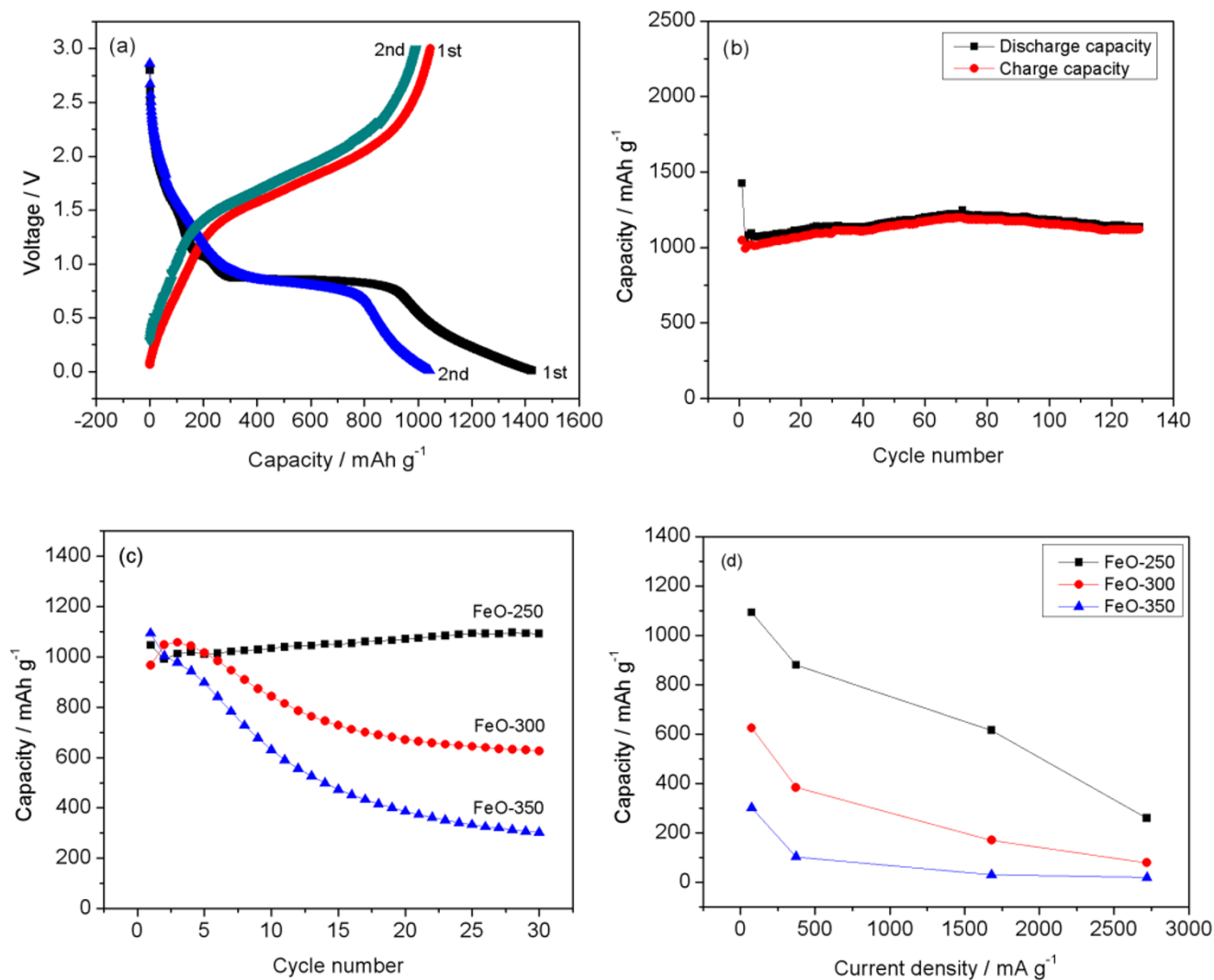
Figure 6 | Electrochemical properties of the iron oxide ribbons for lithium storage. (a) First two discharge-charge curves and (b) cycle performance of FeO-250 ribbons at a current density of 74 mA g^{-1}. (c) Comparisons of the cycle performance of FeO-250, FeO-300 and FeO-350 ribbons during 30 cycles, as well as (d) rate capabilities of FeO-250, FeO-300 and FeO-350 ribbons at the current densities of 74, 372, 1680 and 3720 mA g^{-1} after 30 cycles.

plateau at ~0.8 V can be attributed to the further lithium insertion and conversion of Fe (II) to Fe (0) and associated formation of Li_2O, which is almost the same as that reported for nanostructured iron oxides[4,21,23]. The second slope below 0.8 V should partially arise from the decomposition of electrolyte, and partially from the lithium storage on the surface or at the edges of the iron oxide ribbons owing to their high surface area[24]. This phenomenon commonly becomes dominant with increasing surface area of nanostructured iron oxides[4,6,25]. Thereby, a highly reversible capacity of 1046 mAh g^{-1} for FeO-250 ribbons is obtained during the initial charging process. Remarkably, the reversible charge capacity can be maintained nearly 100% after 130 cycles (Figure 6b), representative of an excellent retention property. Apparently, such a high electrochemical performance of FeO-250 ribbons is superior to some of the previously reported iron oxide-based nanomaterials, including iron oxide nanotubes[26], iron oxide/carbon composites[6,9,20] and pure ion oxide ribbons (Figure S8) obtained under the similar testing conditions. The enhanced electrochemical properties of iron oxide ribbons can be attributed to their unique nanostructure including the finite lateral size and enhanced open-boundaries, which can 1) facilitate lithium ion diffusion through the active material, and 2) decrease the overvoltage of the overall electrode, thus driving a fast electrode reaction during the cycle processes.

The influence of the annealing temperature on the electrochemical performance of FeO ribbons is further explored because the annealing temperature can effectively tailor the nanostructure including porous structure and crystal size in FeO ribbons (Figure 6). Clearly, when increasing the annealing temperature from 250 to 350°C, the capacity retention significantly decreases, although their first reversible capacity is similar (about 1000 mAh g^{-1}) (Figure 6c). In the case of FeO-350, the reversible capacity is rapidly decreased to 302 mAh g^{-1} after 30 cycles. More importantly, the rate capabilities of iron oxide ribbons are strongly dependent on the annealing temperature (Figure 6d and Figure S9). For instance, at a high current density of 1860 mA g^{-1}, a capacity of 615 mAh g^{-1} can be achieved for FeO-250. This value is much higher than those of FeO-300 (170 mAh g^{-1}) and FeO-350 (30 mAh g^{-1}) under the same testing conditions (Figure 6d and Figure S9). To gain more insight, AC impedance measurements of the FeO electrodes were performed after 30 cycles. Their Nyquist plots (Figure 7) show that the diameter of the semicircle for FeO-250 electrode in the high-medium frequency region is much smaller than those of other electrodes, suggesting that FeO-250 electrode possess much lower contact and charge-transfer resistances. The exact kinetic differences among the iron oxide ribbons were inspected by modeling AC impedance spectra based on the modified Randles equivalent circuit (Figure
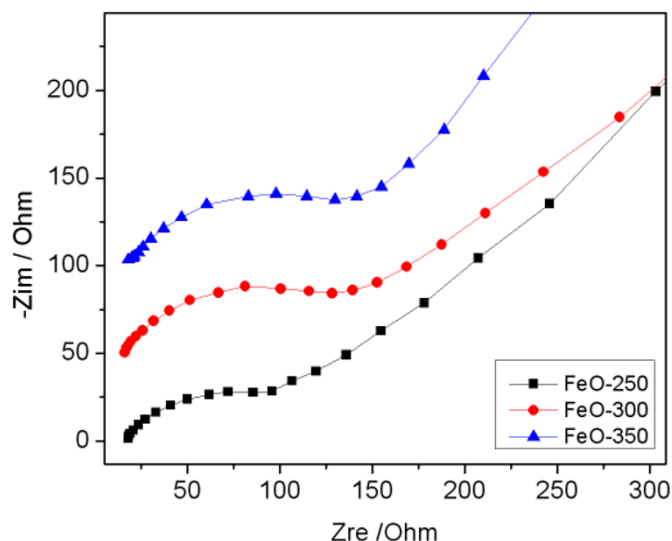
Figure 7 | Electrochemical impedance spectra of the iron oxide ribbon electrodes. Comparison of the Nyquist plots of FeO-250, FeO-300 and FeO-350 electrodes obtained by applying a sine wave with amplitude of 5.0 mV over the frequency range from 100 kHz to 0.01 Hz.

S10)[27,28] and summarized in Figure S1. The values of the Ohmic resistance and charge-transfer resistance are 34.0 and 15.2 Ohm, respectively, for FeO-250 ribbons, which are significantly lower than those of FeO-300 (54.7 and 15.9 Ohm) and FeO-350 (70.6 and 29.8 Ohm) ribbons. These results suggest that the nanostructure of iron oxide ribbons controlled by the annealing temperatures affects not only the electrical conductivity of the overall electrode, but also the electrochemical activity of iron oxide towards lithium during the cycling processes.

Discussion

In summary, we have developed a simple approach to fabricate porous iron oxide ribbons by controlling the nucleation and growth of iron precursors onto the surface of graphene and subsequent thermal annealing in air. The unique structural features of these iron oxide ribbons including the finite lateral size, high surface area, porous structure and enhanced open-edges, lead to the superior electrochemical performance in terms of specific capacity and cycle performance when they are used as anode materials for lithium storage. We believe that such a straightforward and low-cost protocol will provide a new pathway for the large-scale production of various functional materials with controllable morphology and nanostructure for energy storage and conversions.

Methods

Fabrication of graphene oxide and reduced graphene oxide. Graphene oxide was synthesized from natural graphite flakes by the Hummers method[29], the details of which have been described elsewhere[30]. Chemically reduced graphene oxide was prepared as following[31]: in a typical procedure, 25 mg of graphene oxide was dispersed into the solution mixed with 100 ml of water, 50 ml of hydrazine solution (35 wt%) and 350 ml of ammonia solution (28 wt%). After being vigorously stirred for a few minutes, the dispersion was heated to 95°C for 1 h.

Fabrication of porous iron oxide ribbons. Above chemically reduced graphene oxide was first dispersed in a solution of ethylene glycol to create a dark suspension with a concentration of 0.1 wt% by the aid of polyvinylpyrrolidone. The suspension was then mixed with iron (II) acetylacetonate (FeAa) via ultrasonication, in which the weight ratio between reduced graphene and FeAa was fixed to 1:11. After sonication for 3 h, the dispersion was heated to 170°C for the heterogeneous nucleation of the iron glycolate (FeG) onto the surface of reduced grapheme oxide. As increasing the reaction time from 30 min to 5 h, the nucleuses were gradually replaced by the iron glycolate ribbons with increasing lengths. Subsequent thermal annealing of the resulting iron glycolate ribbons at different temperatures (250–400°C) with the heating rate of 2°C/min in air afforded the porous iron oxide ribbons.

Morphology and structure studies. The morphology, microstructure and composition of the samples were investigated by SEM (LEO 1530), TEM (Philips EM 420), HRTEM (Philips F20), AFM (Veeco Dimension 3100), XRD and TGA measurements. The content of iron oxide ribbons in the composite was calculated by subtracting the weight increase from the conversion of Fe_3O_4 to Fe_2O_3 during the TGA process in air. Nitrogen sorption isotherms and BET surface area were measured at 77 K with a Micromeritcs Tristar 3000 analyzer (USA). The Raman spectra were obtained on Lab-RAM HR800 with excitation by an argon ion laser (514.5nm).

Preparation of electrodes and cells. The working electrodes were prepared by mixing the FeO ribbons, carbon black and poly(vinyl difluoride) (PVDF) at a weight ratio of 80:10:10 and pasted on pure Cu foil. Pure lithium foil (Aldrich) was used as the counter electrode. The electrolyte consisted of a solution of 1 M $LiPF_6$ in ethylene carbonate (EC)/dimethyl carbonate (DMC) (1:1 by volume) obtained from Ube Industries Ltd. The standard R2032 type coin cells were assembled in an argon-filled glove box.

Electrochemical performance tests. Galvanostatical discharge-charge experiments were performed at different current densities in the voltage range of 0.01–3.00 V. All the specific capacities of iron oxide ribbons were calculated based on the total mass of the composites. Electrochemical impedance spectroscopy (EIS) measurements of the electrodes were carried out on an electrochemical workstation (PARSTAT 2273). The impedance spectra were recorded by applying a sine wave with amplitude of 5.0 mV over the frequency range from 100 kHz to 0.01 Hz. Fitting of the impedance spectra to the proposed equivalent circuit was performed by the code Z view.

1. Taberna, L., Mitra, S., Poizot, P., Simon, P. & Tarascon, J. M. High rate capabilities Fe_3O_4-based Cu nano-architectured electrodes for lithium-ion battery applications. *Nature Mater.* **5**, 567–573 (2006).
2. Poizot, P., Laruelle, S., Grugeon, S., Dupont, L. & Tarascon, J. M. Nano-sized transition-metaloxides as negative-electrode materials for lithium-ion batteries. *Nature* **407**, 496–499 (2000).
3. Shi, Y. F. *et al.* Ordered mesoporous metallic MoO_2 materials with highly reversible lithium storage capacity. *Nano Lett.* **9**, 4215–4220 (2009).
4. Ban, C. M. *et al.* Nanostructured Fe_3O_4/SWNT electrode: binder-free and high-rate Li-ion anode. *Adv. Mater.* **22**, E145–E149 (2010).
5. Zhu, X. J., Zhu, Y. W., Murali, S., Stollers, M. D. & Ruoff, R. S. Nanostructured reduced graphene Oxide/Fe_2O_3 composite as a high-performance anode material for lithium ion batteries. *Acs Nano* **5**, 3333–3338 (2011).
6. Kang, E. *et al.* Fe_3O_4 Nanoparticles confined in mesocellular carbon foam for high performance anode materials for lithium-ion batteries. *Adv. Funct. Mater.* **21**, 2430–2438 (2011).
7. Chen, J. S., Zhu, T., Yang, X. H., Yang, H. G. & Lou, X. W. Top-down fabrication of alpha-Fe_2O_3 single-crystal nanodiscs and microparticles with tunable porosity for largely improved lithium storage properties. *J. Am. Chem. Soc.* **132**, 13162–13164 (2010).
8. Zhu, T., Chen, J. S. & Lou, X. W. Glucose-assisted one-pot synthesis of FeOOH nanorods and their transformation to Fe3O4@carbon nanorods for application in lithium ion batteries. *J. Phys. Chem. C* **115**, 9814–9820 (2011).
9. Zhang, W. M., Wu, X. L., Hu, J. S., Guo, Y. G. & Wan, L. J. Carbon coated Fe_3O_4 nanospindles as a superior anode material for lithium-ion batteries. *Adv. Funct. Mater.* **18**, 3941–3946 (2008).
10. Wang, G. X., Shen, X. P., Yao, J. & Park, J. Graphene nanosheets for enhanced lithium storage in lithium ion batteries. *Carbon* **47**, 2049–2053 (2009).
11. Zhang, Y. J., Lu, J., Shen, S. L., Xu, H. R. & Wang, Q. B. Ultralarge single crystal SnS rectangular nanosheets. *Chem. Commun.* **47**, 5226–5228 (2011).
12. Seo, J. W. *et al.* Two-dimensional nanosheet crystals. *Angew. Chem. Int. Ed.* **46**, 8828–8831 (2007).
13. Gao, J., Lowe, M. A. & Abruna, H. D. Spongelike nanosized Mn_3O_4 as a high-capacity anode material for rechargeable lithium batteries. *Chem. Mater.* **23**, 3223–3227 (2011).
14. Bhardwaj, T., Antic, A., Pavan, B., Barone, V. & Fahlman, B. D. Enhanced electrochemical lithium storage by graphene nanoribbons. *J. Am. Chem. Soc.* **132**, 12556–12558 (2010).
15. Uthaisar, C., Barone, V. & Peralta, J. E. Lithium adsorption on zigzag graphene nanoribbons. *J. Appl. Phys.* **106**, 113715 (2009).
16. Yang, S. B. *et al.* Graphene-based nanosheets with a sandwich structure. *Angew. Chem. Int. Ed.* **49**, 4795–4799 (2010).
17. Yang, S. B., Feng, X. L. Wang, X. C. & Müllen, K. Graphene-based carbon nitride nanosheets as efficient metal-free electrocatalysts for oxygen reduction reactions. *Angew. Chem. Int. Ed.* **50**, 5339–5343 (2011).
18. Wang, H. L., Casalongue, H. S., Liang, Y. Y. & Dai, H. J. $Ni(OH)_2$ nanoplates grown on graphene as advanced electrochemical pseudocapacitor materials. *J. Am. Chem. Soc.* **132**, 7472–7477 (2010).
19. Wang, H. L., Robinson, J. T., Diankov, G. & Dai, H. J. Nanocrystal growth on graphene with various degrees of oxidation. *J. Am. Chem. Soc.* **132**, 3270–3271 (2010).
20. Zhou, G. M. *et al.* Graphene-wrapped Fe_3O_4 anode material with improved reversible capacity and cyclic stability for lithium ion batteries. *Chem. Mater.* **22**, 5306–5313 (2010).

21. Zhou, W. *et al.* Hierarchial mesoporous hematite with "electron-transport channels" and its improved performances in photocatalysis and lithium ion batteries. *J. Phys. Chem. C* **115**, 7126–7133 (2011).

22. Sun, B. H. *et al.* Synthesis of mesoporous alpha-Fe₂O₃ nanostructures for highly sensitive gas sensors and high capacity anode materials in lithium ion batteries. *J. Phys. Chem. C* **114**, 18753–18761 (2010).

23. Zhou, J. S. *et al.* Carbon-encapsulated metal oxide hollow nanoparticles and metal oxide hollow nanoparticles: A general synthesis strategy and its application to lithium-ion batteries. *Chem. Mater.* **21**, 2935–2940 (2009).

24. Yang, S. B., Feng, X. L. & Müllen, K. Sandwich-Like, graphene-based titania nanosheets with high surface area for fast lithium storage. *Adv. Mater.* **23**, 3575–3579 (2011).

25. Wu, C. Z., Yin, P., Zhu, X., Ouyang, C. Z. & Xie, Y. Synthesis of hematite (alpha-Fe₂O₃) nanorods: diameter-size and shape effects on their applications in magnetism, lithium ion battery, and gas sensors. *J. Phys. Chem. B* **110**, 17806–17812 (2006).

26. Wang, Z. Y., Luan, D. Y., Madhavi, S., Li, C. M. & Lou, X. W. alpha-Fe₂O₃ nanotubes with superior lithium storage capability. *Chem. Commun.* **47**, 8061–8063 (2011).

27. Yang, S. B., Feng, X. L., Ivanovici, S. & Müllen, K. Fabrication of graphene-encapsulated oxide nanoparticles: towards high-performance anode materials for lithium storage. *Angew. Chem. Int. Ed.* **49**, 8408–8411 (2010).

28. Yang, S. B. *et al.* Nanographene-constructed hollow carbon spheres and their favorable electroactivity with respect to lithium storage. *Adv. Mater.* **22**, 838–842 (2010).

29. Hummers, W. S. & Offeman, R. E. Preparation of graphitic oxide. *J. Am. Chem. Soc.* **80**, 1339–1339 (1958).

30. Liang, Y. Y. *et al.* Transparent, highly conductive graphene electrodes from acetylene-assisted thermolysis of graphite oxide sheets and nanographene molecules. *Nanotechnology* **20**, 434007 (2009).

31. Li, D., Müller, M. B. Gilje, S., Kaner, R. B. & Wallace, G. G. Processable aqueous dispersions of graphene nanosheets. *Nature Nanotechn.* **3**, 101–105 (2008).

Acknowledgements

Author contributions

S.B.Y. carried out the experiments (synthesis, SEM, TEM, AFM, XRD and electrochemical tests) and wrote the paper. S. Y. and Y. H. conducted the HRTEM measurements. L. C. conducted BET measurements. All the results were discussed with X. L. F. and K. M. All authors contributed to revision of the manuscript.

Additional information

Supplementary information accompanies this paper at http://www.nature.com/scientificreports

Competing financial interests The authors declare no competing financial interests.

How to cite this article: Yang, S. *et al.* Porous Iron Oxide Ribbons Grown on Graphene for High-Performance Lithium Storage. *Sci. Rep.* **2**, 427; DOI:10.1038/srep00427 (2012).